PAPER

In situ identification of crystal facet-mediated chemical reactions on tetrahexahedral gold nanocrystals using surface-enhanced Raman spectroscopy†

Xiufeng Lang,[ab] Tingting You,[a] Penggang Yin,*[a] Enzhong Tan,[a] Yan Zhang,[a] Yifan Huang,[c] Hongping Zhu,[c] Bin Ren[c] and Lin Guo*[a]

Direct monitoring of a metal-catalyzed reaction by surface-enhanced Raman scattering (SERS) is always a challenging issue as it needs bifunctional metal structures that have plasmonic properties and also act as catalysts. Here we demonstrate that the tetrahexahedral (THH) gold nanocrystals (Au NCs) with exposed {520} facets give highly enhanced Raman signals from molecules at the interface, permitting *in situ* observation of chemical transformation from *para*-aminothiophenol (PATP) to 4,4′-dimercaptoazobenzene (DMAB). The origin of the intense SERS signals of DMAB is carefully investigated based on the comparison of the SERS spectra of PATP obtained with both the THH Au NCs and the Au nanospheres with the exposed {111} facets. It is elucidated that the high-index {520} facet rather than the localized surface plasmons of the THH Au NCs plays a key role in producing a high yield of the product DMAB which is accompanied by the selective enhancement of the characteristic Raman signals.

1. Introduction

Determining the catalytic activity and the reaction kinetics is a key issue when new catalysts are developed, characterized and introduced. In principle, reactions at the surface of metal structures can be studied using molecular surface specific spectroscopic techniques.[1,2] Among these, surface-enhanced Raman scattering (SERS), which combines the advantages of high chemical specificity[3] (vibrational Raman scattering), high sensitivity[4] (electromagnetic and chemical enhancement), and surface-selectivity[5] (near-field enhancement), has been widely applied in investigations of different types of reactions at electrochemical interfaces[6] and metal surfaces[7–11] *in situ* to probe, for example, the formation of reaction intermediates[6] and photoreaction kinetics of isolated reactants.[8,10] In order to investigate a metal-catalyzed reaction with SERS, bifunctional metal structures are needed that have plasmonic properties and also act as catalysts,[12] so direct observation of a catalytic process by SERS has been rare.[9–11] Previous studies employed composite

structures with plasmonic (Au) and catalytic (Pd or Pt) properties to monitor the catalytic reactions by SERS.[5,9,10] It has been well established that the gold nanoparticles (Au NPs) exhibit high catalytic activity and strong plasmonic properties, providing a good candidate for SERS monitoring of gold-catalyzed reaction. However, the central dilemma is that Au NPs smaller than 10 nm exhibit catalytic activity but weak SERS activity,[13] while Au NPs larger than 20 nm exhibit efficient SERS activity but no catalytic activity.[14] Very recently, Xie *et al.* reported a rational chemical approach for integrating catalytically active small Au NPs with SERS-active large Au NPs into a single bifunctional metal superstructure to realize SERS monitoring of chemical reactions catalyzed by Au NPs.[11] Herein we demonstrate that high-index faceted Au NPs can be used to probe directly the gold-catalyzed reactions by using SERS.

The high-index-faceted Au NCs have shown greatly enhanced performance for specific catalytic reactions relative to those bound by low-index facets,[15] because high-index facets have high densities of atom steps and kinks on them, which serve as active sites for breaking chemical bonds.[16] Furthermore, some high-index faceted Au NCs, such as tetrahexahedral (THH) Au NCs,[17] and hexoctahedral (HOH) Au NCs,[18] have also been reported to exhibit efficient SERS activities due to the presence of large numbers of well-defined tips, edges, and intraparticle gaps on their surfaces, which can serve as hot spots for large electric-field enhancement and thus give strong SERS signals. Prompted by the previous studies, we investigate chemical transformation from *para*-aminothiophenol (PATP) to 4,4′-dimercaptoazobenzene

[a] *Key Laboratory of Bio-inspired Smart Interfacial Science and Technology of Ministry of Education, School of Chemistry and Environment, Beihang University, Beijing, China. E-mail: pgyin@buaa.edu.cn, guolin@buaa.edu.cn*
[b] *Beijing Computational Science Research Center, Beijing, China*
[c] *Department of Chemistry, College of Chemistry and Chemical Engineering, Xiamen University, Xiamen, China*

This journal is © the Owner Societies 2013

Phys. Chem. Chem. Phys., 2013, **15**, 19337–19342 | **19337**

(DMAB) on the THH Au NCs with exposed {520} facets by recording the fingerprints of these molecules with SERS. Further, we measure and compare the reaction efficiencies of PATP on the THH Au NCs and rough Au nanospheres with exposed {111} facets. The observed differences in the reaction efficiencies on these two types of Au NCs elucidate that crystal facets endow the THH Au NCs with excellent enhanced catalytic activity.

2. Experimental section

2.1 Sample preparation and characterization

THH Au NCs were prepared using a seed-mediated growth method developed by our group.[19] In brief, cetyltrimethyl-ammonium bromide (CTAB)-capped gold seed solution was prepared by injecting $NaBH_4$ solution into the mixture of CTAB and $HAuCl_4$. Then, 0.3 mL of seed solutions was added into the growth solution containing didodecyldimethylammonium bromide (DDAB) (0.005 M, 5 mL), $HAuCl_4$ (0.001 M, 5 mL), $AgNO_3$ (0.01 M, 100 μL) and ascorbic acid (AA) (0.1 M, 80 μL) to fabricate quasi-THH Au NCs. The precipitate of quasi-THH Au NCs was then dispersed in deionized water and used as a precursor in preparation of the THH Au NCs. To prepare the THH Au NCs, 0.0729 g of CTAB was dissolved in DDAB (0.01 M, 5 mL) to make a binary surfactant. To this solution, $HAuCl_4$, $AgNO_3$, H_2SO_4 (0.5 M, 40 μL) and AA (0.1 M, 80 μL) were sequentially added, and then, the quasi-THH Au NCs solution (50 μL) was injected. The final solution was kept at 30 °C overnight to obtain the THH Au NCs. The Au nanospheres were prepared in dimethyl sulfoxide aqueous solution. Cetyltri-methylammonium chloride (CTAC)-capped gold seed solution was first prepared by injecting $NaBH_4$ solution into the mixture of CTAC and $HAuCl_4$. Then, 12 μL of seed solution was added to the growth solution containing CTAB (0.2 M, 6.75 μL), poly-vinylpyrrolidone (PVP) (0.001 M, 1.35 mL), $HAuCl_4$ (0.0005 M, 2.7 mL), ethanediol (7 mL), and AA (0.05 M, 100 μL). The final solution was put into a 30 °C water bath overnight. The Au nano-spheres were washed three times by centrifugation (12 000 rpm, 5 min) for characterization.

The general morphologies of the as-prepared nanocrystals were characterized using a field-emission-gun scanning electron microscope (SEM) (Hitachi S-4800, 5 kV). To evaluate the Raman spectra, the substrate was prepared by dropping 10 μL of the samples (THH Au NCs or Au nanospheres) onto a carefully cleaned silicon wafer and allowed to dry naturally in air. After repeating the dropping 3×, the substrate was immersed into $1 × 10^{-3}$ mol L^{-1} PATP ethanol solution over 24 hours to ensure binding of PATP on the Au NPs. After thoroughly rinsing with absolute ethanol several times to remove the free PATP molecules and drying in the dark at room temperature, it was subjected to Raman characterization using a Raman spectrometer. Raman spectra were recorded on a Jobin Yvon (Laboratory RAM HR800) confocal micro-Raman spectrometer. An internal He–Ne laser emitting at a wavelength of 632.8 nm was used as a source of excitation. The scattered light was analyzed using a Dilor XY triple spectrometer and a liquid-nitrogen-cooled CCD multichannel detector. The Raman band of a silicon wafer at 520 cm^{-1} was

used to calibrate the spectrometer. The spectra were obtained by using a 50× objective lens to focus the laser beam onto a spot with ∼1 μm diameter.

2.2 Computational methods

To extract the adsorption structure and simulate Raman spectra of PATP and DMAB adsorbed on the Au NCs, we model PATP and DMAB bound to Au NCs as the molecules bonded to Au_n ($n = 1, 3, 5, 13$ and 19) clusters through the strong S–Au bond. Geometry optimization and vibrational frequency calculations were carried out with generalized gradient approximation (GGA) for exchange–correlation functional PW91PW91.[20] For C, N, S, and H atoms, the basis sets were 6-31G(d) and for the Au atom, the valence electrons and the inner shells were described by the basis set, LANL2DZ, and the corresponding relativity effective core potentials, respectively.[21] All the quantum chemical calcula-tions were performed using the Gaussian 03 package.[22] Based on the Raman activity obtained from the Guassian package, absolute Raman intensities are calculated on top of the differential Raman scattering cross section in order to make direct comparison with the above Raman experiments.[23]

In order to compare the electric field (E-field) near the THH Au NCs and the Au nanospheres, a theoretical simulation was carried out by using a 3-dimensional finite-difference time-domain (3D-FDTD) method.[24] Models in this work were constructed according to the scanning electron microscopy (SEM) images of these Au NPs. The THH nanocrystal model was constructed by an 100 nm × 100 nm × 100 nm cubic body and 20 nm height pyramids on top of each facet. The nano-sphere model with coarse surfaces has a diameter of 140 nm and was modeled by a flower-like nanoparticle with several protuberances on its surface. Incident plane wave was propa-gated from the z axis and was polarized along the x direction. The wavelength was set at 633 nm in all simulations. Data of dielectric constants were from Johnson and Christy.[25] The Yee cell size in FDTD simulation was carefully considered to meet the accuracy needed by both wavelength and object parameters and to avoid too large memory resources and computation time required. Thus, 1 nm × 1 nm × 1 nm mesh was applied over the object region.

3. Results and discussion

3.1 Transformation from PATP to DMAB on the THH Au NCs

Our initial investigation is based on a synthetic system for the THH Au NCs developed by our group.[19] The THH Au NC has an average size of 150 nm and is enclosed by 24 high-index {520} facets (Fig. 1a and see ref. 19 for structural details). It has been reported that the THH Au NCs can exhibit high catalytic performance toward the electro-oxidation of formic acid[19] and large Raman efficiency of the probe p-mercapto benzoic acid (PMBA).[17] Based on this cognition, we directly probe the synthesis of the azo compounds from anilines catalyzed by the THH gold NCs using SERS. Specifically, educt of the reaction is a self-assembled monolayer of PATP on the surface of the THH Au NCs. Fig. 1b shows the normal Raman spectrum (NRS) of
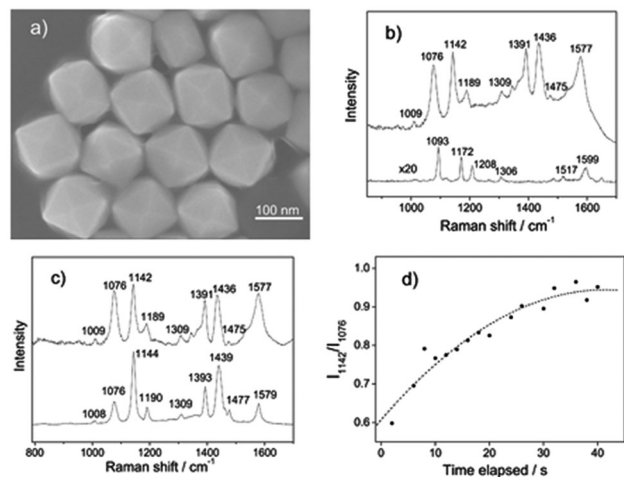
19338 | Phys. Chem. Chem. Phys., 2013, **15**, 19337–19342

This journal is © the Owner Societies 2013

Fig. 1 (a) SEM image of THH Au NCs. (b) Normal Raman spectrum of PATP powder (bottom line) and the SERS spectrum of PATP adsorbed on THH Au NCs (top line). The laser power was 1.6 mW and the acquisition time was 2 s. (c) SERS spectra of DMAB (bottom line) and PATP (top line) adsorbed on THH Au NCs. (d) Time dependent relative Raman intensity between the 1142 cm^{-1} and 1076 cm^{-1} bands. The laser power was 0.2 mW and the acquisition time was 2 s in (c) and (d).

Fig. 2 (A) Optimized geometries of (a) PATP molecule, (b) PATP–Au$_5$ complex, (c) DMAB molecule and (d) DMAB–Au$_5$ complex. Herein, the N and S atoms are linked by two white H atoms and a white H atom in the PATP, respectively. In the complexes, two Au atoms are connected by the S atom. (B) The corresponding simulated Raman spectra. A linewidth of 10 cm^{-1} in the Lorentzian line shape was used to calculate the Raman spectra.

PATP powder and the SERS spectrum of PATP adsorbed on the Au NCs. Compared to the NRS, the most noticeable differences in the SERS spectrum are the frequency shifts and changes in relative intensity for most Raman-active bands. In previous studies, the bands at 1076, 1189 and 1577 cm^{-1}, assigned to a_1 modes, were considered to be the red shift bands of the Raman-active bands at 1093, 1208, and 1599 cm^{-1} in NRS, and three new bands at 1142, 1391 and 1436 cm^{-1}, assigned to b_2 modes, were usually proposed to be originated from the photon-driven charge transfer mechanism.[26–28] However, recent studies suggested that these new bands may be originated from the species DMAB, which is produced from the oxidation of PATP on roughened Ag electrodes or Ag NPs.[29,30] In spite of these studies, the transformation from PATP to DMAB is not well understood on the Au substrates.

Herein, we compared the SERS features of DMAB adsorbed on the THH Au NCs (synthesized by Huang et al.[7]) with that obtained from the above mentioned PATP system. Both spectra have essentially identical spectral features (Fig. 1c), which convincingly demonstrate that they are from the same species. Thus, DMAB species were successfully synthesized from PATP on the THH Au NCs. This is supported by the oxidative formation of azo species from aniline group molecules in the presence of oxide-supported Au nanocatalysts.[31] The experimental result is also in accord with the theoretical simulation where density functional theory is used to calculate SERS spectra of PATP–Au and DMAB–Au systems. The simulated result clearly shows that only the DMAB–Au system can produce the SERS profile of PATP adsorbed on the THH Au NCs, supporting the above chemical transformation from PATP to DMAB (see Fig. 2A and Fig. S1, ESI† for model structures and Fig. 2B and Fig. S2, ESI† for calculated Raman spectra). Furthermore, we used the relative Raman intensity of the
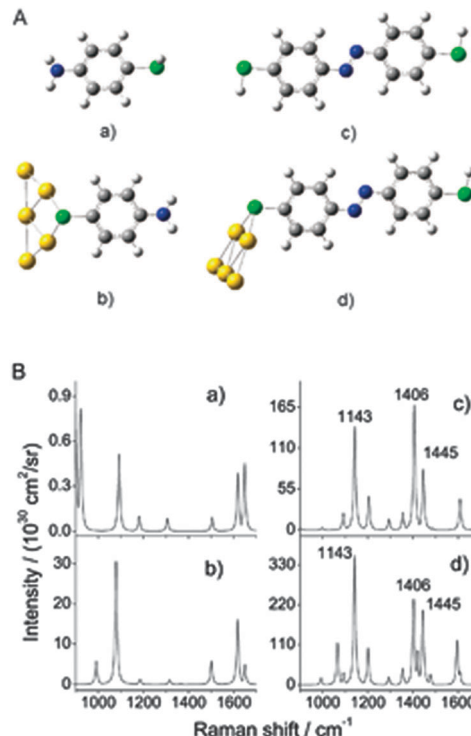
1142 cm^{-1} band with respect to the 1076 cm^{-1} band as a quantitative measure of the reaction progress. The choice of these two bands is based on the previous reports that the bands at 1142, 1391 and 1436 cm^{-1} were exclusively produced by new species DMAB, and the band at 1076 cm^{-1} was mainly produced by the reactant PATP.[7,9] Time evolution of the relative Raman intensity in Fig. 1d shows that it increases drastically from 0.6 to 0.9 within the initial 30 seconds when using the laser power of 0.2 mW, and during the next 10 seconds, it increases slowly (the change is less than 10%). This shows that most of the DMAB species could be produced within 30 seconds in the catalytic process. Of note, we also observed that more DMAB species are yielded on the THH Au NCs within shorter time when higher laser power (1.6 mW) is used (data are not shown here). Similar spectral features have been reported in the SERS measurement of PATP adsorbed on small Au nanospheres, where the relative Raman intensity increased from 0.4 to 0.8 within 180 seconds when using the laser power of 0.65 mW in the previous work.[32] Based on a large difference in relative Raman intensities of PATP adsorbed on both the THH Au NCs and Au nanospheres, it is found that the reaction efficiency and kinetics on the THH Au NCs are larger and faster than the Au nanospheres, respectively. The physics of the mechanism behind such a difference will be discussed in the following study.

3.2 Effects of crystal facets on the chemical transformation

Given that selectively enhanced Raman signals at 1142, 1391 and 1436 cm^{-1} bands, characterizing large reaction efficiency of DMAB, can be observed on the THH Au NCs as compared to weak Raman signals obtained on Au NPs,[32–34] it is fundamentally interesting to elucidate the mechanism behind what factor induces the change in Raman intensity of new bands and thus the reaction efficiency of DMAB. The THH Au NCs have been demonstrated to exhibit intense localized surface plasmon resonance (LSPR) effects due to their large size and special shape.[17] It is possible that intense Raman signals at these bands may be produced by LSPR effects of the Au NCs, *i.e.*, electromagnetic enhancement of SERS.[35] Furthermore, some reports suggested that LSPR could improve the chemical transformation from PATP to DMAB on metal nanoparticles such as Ag or Cu NPs.[31,36] Thus, high LSPR intensity of the THH Au NCs possibly facilitates the synthesis of DMAB on the surfaces, and leads to more DMAB species on the Au NCs than those on the Au NPs. To assess the LSPR effects of the characteristic bands of DMAB, we synthesized rough Au nanospheres with an average size of 140 nm and exposed low-index {111} facets (see ESI,† Fig. S3 and S4 for structural details) and measured the SERS spectra of PATP adsorbed on the THH Au NCs and the Au nanospheres for comparison. The UV-vis spectra features of the Au nanospheres are similar to those of the THH Au NCs (see ESI,† Fig. S5), eliminating a possible effect of degree of overlap between the peak of surface plasmon resonance for the nanocrystals and the excitation source on SERS activity. To gain more insight into their LSPR characteristics, the electric-field (E-field) amplitude distributions near the surface of the THH Au NCs and Au nanospheres were computed using the 3-dimensional finite difference time-domain (3D-FDTD) method. The simulated E-field amplitude ($|E|$) distributions clearly show that the THH Au NCs and the Au nanospheres give the largest E-field amplitude ($|E_{max}|$ = 91 and 61) at the tips and the protuberances, respectively (see Fig. 3a–d), and comparable average E-field intensities near their surfaces. These results prove that the THH Au NCs and the Au nanospheres have similar LSPR effects. However, the measured relative Raman intensities at

1142, 1391 and 1436 cm^{-1} in the SERS spectrum of PATP adsorbed on the Au nanospheres are much smaller than those on the THH Au NCs (see Fig. 2c). We therefore conclude that the LSPR produces enhanced Raman signals in SERS spectra of DMAB formed on the THH Au NCs, but cannot explain the selective enhancement of the characteristic bands at 1142, 1391 and 1436 cm^{-1}.

Since the large Raman intensities of three bands are irrelevant to the LSPR, we have to reexamine the nature of the THH Au NCs from the viewpoint of their direct interactions with PATP. As mentioned in the introduction, the THH Au NCs were expected to exhibit high catalytic activity due to their high-index {520} facets. To demonstrate the possibility that the crystal facet plays a critical role in selectively promoting the signal intensities of the bands, we quantitatively investigated the transformation of PATP into DMAB on the THH Au NCs and the rough Au nanospheres. We dropped the THH Au NCs and the Au nanospheres, both capped by PATP molecules, onto two labeled silicon wafers, and chose monolayers of twenty THH gold NCs (Fig. 4a) and forty gold nanospheres (Fig. 4b) to measure the SERS spectra of PATP. As shown in Fig. 4c, intense SERS signals of 1142, 1391 and 1436 cm^{-1} bands are clearly observed for the THH Au NCs, while negligible signals are obtained for the Au nanospheres. We denoted the relative Raman intensity of 1142 cm^{-1} band per surface atom per second as a measure of the turnover frequency (TOF) in the reaction to quantify catalytic activities of two types of the Au NPs (see ESI,† Section S1 for calculation details). The TOF of the THH Au NCs (2.73×10^{-9} s^{-1}) is two times larger than that of the Au nanospheres with a smooth surface (1.16×10^{-9} s^{-1}). Note that if the rough surface is considered for the Au nanospheres, total surface atoms on a single nanosphere should increase, and the actual TOF number is lower than 1.16×10^{-9} s^{-1}. The large reaction rate difference clearly demonstrates that the
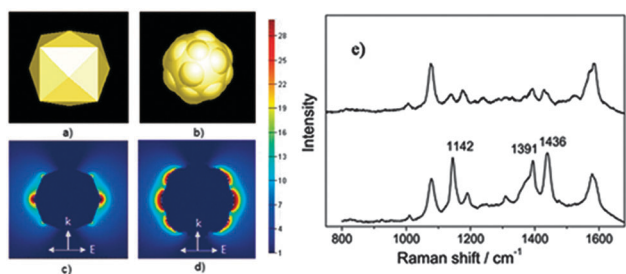

Fig. 3 (a and b) 3D-FDTD-simulation models for calculating the $|E|$ distributions of the 154 nm THH Au NCs and 140 nm Au nanospheres. (c and d) $|E|$ distributions of the (c) THH Au NCs and (d) Au nanospheres. E-field amplitude in the *XZ* plane was plotted. (e) SERS spectra of PATP obtained with both THH Au NCs (bottom line) and the Au nanosphere (top line). The laser power was 0.2 mW and the acquisition time was 20 s.
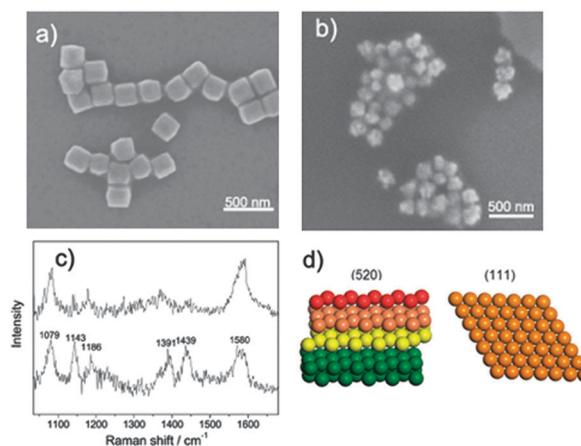

Fig. 4 SEM images of the (a) PATP-capped THH Au NCs and (b) PATP-capped Au nanospheres on labeled silicon wafers. (c) Corresponding SERS spectra of PATP obtained with both THH Au NCs (bottom line) and spherical Au NCs (top line). The laser power was 0.2 mW and the acquisition time was 20 s. (d) Structural models of {520} and {111} facets for the THH Au NCs and the Au nanospheres. For {520} facets, depth of the colour represents step atoms on different layers.

19340 | *Phys. Chem. Chem. Phys.*, 2013, **15**, 19337–19342

This journal is © the Owner Societies 2013

catalytic performance of the THH gold NCs is better than that of the Au nanospheres. The excellent catalytic activity of the THH Au NCs should be attributed to their possession of high-index {520} facets. Such crystal surfaces have a large number of Au step atoms, while the low-index {111} surfaces only have atoms at terrace (Fig. 4d). The step atoms provide more active sites on the THH Au NCs to readily adsorb PATP molecules and then produce DMAB under laser illumination, which is revealed by greatly enhanced signals of 1142, 1391 and 1436 cm^{-1} bands. Thus, due to the large size and high-index facets, the THH Au NCs can provide large plasmonic properties and high catalytic activity to *in situ* probe surface reaction catalyzed by Au NPs.

4. Conclusions

In summary, we have demonstrated that chemical transformation from *p*-aminothiophenol (PATP) to 4,4′-dimercaptoazobenzene (DMAB) can be followed *in situ* using surface-enhanced Raman scattering in proximity to high-index {520} faceted tetrahexahedral (THH) gold nanocrystals (Au NCs), which is supported by density functional calculations. Furthermore, we compared the SERS intensity of PATP adsorbed on THH Au NCs and the Au nanospheres with a similar size but exposed {111} facets. It is found that selective enhancement of the characteristic bands of DMAB is more significant on the Au NCs than the Au nanospheres. The mechanistic studies suggest that the high-index {520} facets rather than the strong localized surface resonance endow the THH Au NCs with enhanced catalytic activity toward the synthesis of DMAB. Recently, many nanocrystals with well-defined facets (such as Ru, Pt and Pd nanocrystals) have been fabricated and demonstrated to exhibit excellent catalytic activity or/and high SERS efficiency,[37–39] so our results may provide a facile route to directly observe the metal-catalyzed reaction on the highly active nanomaterials with SERS.

Notes and references

1 M. Arenz, K. J. J. Mayrhofer, V. Stamenkovic, B. B. Blizanac, T. Tomoyuki, P. N. Ross and N. M. Makovic, *J. Am. Chem. Soc.*, 2005, **127**, 6819.

2 S. Lehwald, H. Ibach and J. E. Demuth, *Surf. Sci.*, 1978, **78**, 577.

3 E. Cortes, P. G. Etchegoin, E. C. L. Ru, A. Fainstein, M. E. Vela and R. C. Salvarezza, *J. Am. Chem. Soc.*, 2010, **132**, 18034.

4 M. Moskovits, *J. Raman Spectrosc.*, 2005, **36**, 485.

5 K. N. Heck, B. G. Janesko, G. E. Scuseria, N. J. Halas and M. S. Wong, *J. Am. Chem. Soc.*, 2008, **130**, 16592.

6 A. Wang, Y. F. Huang, U. K. Sur, D. Y. Wu, B. Ren, S. Rondinini, C. Amatore and Z. Q. Tian, *J. Am. Chem. Soc.*, 2010, **132**, 9534.

7 Y. Huang, H. Zhu, G. Liu, D. Wu, B. Ren and Z. Q. Tian, *J. Am. Chem. Soc.*, 2010, **132**, 9244.

8 Y. B. Zheng, J. L. Payton, T. Song, B. K. Pathem, Y. Zhao, H. Ma, Y. Yang, L. Jensen, A. K.-Y. Jen and P. S. Weiss, *Nano Lett.*, 2012, **12**, 5362.

9 W. Xie, C. Herrmann, K. Kömpe, M. Haase and S. Schlücker, *J. Am. Chem. Soc.*, 2011, **133**, 19032.

10 V. Joseph, C. Engelbrekt, J. Zhang, U. Gernert, J. Ulstrup and J. Kneipp, *Angew. Chem., Int. Ed.*, 2012, **51**, 7592.

11 W. Xie, B. Walkenfort and S. Schlücker, *J. Am. Chem. Soc.*, 2013, **135**, 1657.

12 X. J. Gu and K. L. Akers, *J. Phys. Chem.*, 1992, **96**, 383.

13 B. Hvolbæk, T. V. W. Janssens, B. S. Clausen, H. Falsig, C. H. Christensen and J. K. Nørskov, *Nano Today*, 2007, **2**, 14.

14 J. T. Krug, G. D. Wang, S. R. Emory and S. M. Nie, *J. Am. Chem. Soc.*, 1999, **121**, 9208.

15 Z. Zhou, N. Tian, J. Li, I. Broadwell and S. Sun, *Chem. Soc. Rev.*, 2011, **40**, 4167.

16 N. Tian, Z. Zhou and S. Sun, *J. Phys. Chem. C*, 2008, **112**, 19801.

17 P. Yin, T. You, E. Tan, J. Li, X. Lang and L. Guo, *J. Phys. Chem. C*, 2011, **115**, 18061.

18 J. W. Hong, S. Lee, Y. W. Lee and S. W. Han, *J. Am. Chem. Soc.*, 2012, **134**, 4565.

19 J. Li, L. Wang, L. Guo, X. Han and Z. Zhang, *Chem. Commun.*, 2010, **46**, 5109.

20 J. P. Perdew, K. Burke and Y. Wang, *Phys. Rev. B: Condens. Matter Mater. Phys.*, 1996, **54**, 16533.

21 P. J. Hay and W. R. Wadt, *J. Chem. Phys.*, 1985, **82**, 299.

22 M. J. Frisch, G. W. Trucks, H. B. Schlegel, G. E. Scuseria, M. A. Robb, J. R. Cheeseman, J. A. Montgomery, Jr., T. Vreven, K. N. Kudin, J. C. Burant, J. M. Millam, S. S. Iyengar, J. Tomasi, V. Barone, B. Mennucci, M. Cossi, G. Scalmani, N. Rega, G. A. Petersson, H. Nakatsuji, M. Hada, M. Ehara, K. Toyota, R. Fukuda, J. Hasegawa, M. Ishida, T. Nakajima, Y. Honda, O. Kitao, H. Nakai, M. Klene, X. Li, J. E. Knox, H. P. Hratchian, J. B. Cross, C. Adamo, J. Jaramillo, R. Gomperts, R. E. Stratmann, O. Yazyev, A. J. Austin, R. Cammi, C. Pomelli, J. W. Ochterski, P. Y. Ayala, K. Morokuma, G. A. Voth, P. J. Salvador, J. Dannenberg, V. G. Zakrzewski, S. Dapprich, A. D. Daniels, M. C. Strain, O. Farkas, D. K. Malick, A. D. Rabuck, K. Rahgavachari, J. B. Foresman, J. V. Ortiz, Q. Cui, A. G. Baboul, S. Clifford, J. Cioslowski, B. B. Stefanov, G. Liu, A. Liashenko, P. Piksorz, I. Komaromi, R. L. Martin, D. J. Fox, T. Keith, M. A. Al-Laham, C. Y. Peng, A. Nanayakkara, M. Challacombe, P. M. W. Gill, B. Johnson, W. Chen, M. W. Wong, C. Gonzalez and J. A. Pople, *Gaussian 03 (Revision E.01)*, Gaussian, Inc., Pittsburgh, PA, 2003.

23 X. F. Lang, P. G. Yin, T. T. You, L. Jiang and L. Guo, *ChemPhysChem*, 2011, **12**, 2468.

24 C. Oubre and P. Noldlander, *J. Phys. Chem. B*, 2004, **108**, 17740.

This journal is © the Owner Societies 2013

Phys. Chem. Chem. Phys., 2013, **15**, 19337–19342 | **19341**

25 P. B. Johnson and R. W. Christy, *Phys. Rev. B: Solid State*, 1972, **6**, 4370.

26 M. Osawa, N. Matsuda, K. Yoshii and I. Uchida, *J. Phys. Chem.*, 1994, **98**, 12702.

27 W. Park and Z. H. Kim, *Nano Lett.*, 2010, **10**, 4040.

28 W. Ji, N. Spegazzini, Y. Kitahama, Y. Chen, B. Zhao and Y. Ozaki, *J. Phys. Chem. Lett.*, 2012, **3**, 3204.

29 Y. Huang, D. Wu, H. Zhu, L. Zhao, G. Liu, B. Ren and Z. Q. Tian, *Phys. Chem. Chem. Phys.*, 2012, **14**, 8485.

30 H. Choi, H. Shon, H. Yu, T. G. Lee and Z. H. Kim, *J. Phys. Chem. Lett.*, 2013, **4**, 1079.

31 A. Grirrane, A. Corma and H. García, *Science*, 2008, **322**, 1661.

32 G. Liu, J. Hu, P. Zheng, G. Shen, J. Jiang, R. Yu, Y. Cui and B. Ren, *J. Phys. Chem. C*, 2008, **112**, 6499.

33 X. Hu, T. Wang, L. Wang and S. Dong, *J. Phys. Chem. C*, 2007, **111**, 6962.

34 J. H. Yoon, J. S. Park and S. Yoon, *Langmuir*, 2009, **25**, 12475.

35 J. R. Lombardi and R. L. Birke, *J. Phys. Chem. C*, 2008, **112**, 5605.

36 M. Sun and H. X. Xu, *Small*, 2012, **8**, 2777.

37 K. Zhou and Y. Li, *Angew. Chem., Int. Ed.*, 2012, **51**, 602.

38 Y. W. Lee, M. Kim, S. W. Kang and S. W. Han, *Angew. Chem., Int. Ed.*, 2011, **50**, 3466.

39 A. Yin, W.-C. Liu, J. Ke, W. Zhu, J. Gu, Y. Zhang and C.-H. Yan, *J. Am. Chem. Soc.*, 2012, **134**, 20479.

19342 | *Phys. Chem. Chem. Phys.*, 2013, **15**, 19337–19342

This journal is © the Owner Societies 2013